Geology

Monitoring and forecasting fault development at actively forming calderas: an experimental study

--Manuscript Draft--

Manuscript Number:	G39551R1
Full Title:	Monitoring and forecasting fault development at actively forming calderas: an experimental study
Short Title:	Monitoring and forecasting fault development at actively forming calderas
Article Type:	Article
Keywords:	Calderas, faults, monitoring, analogue experiments, sandbox, propagation rate, piezoelectric sensor, stress
Corresponding Author:	Gilles Seropian University of Bristol School of Earth Sciences Bristol, Avon UNITED KINGDOM
Corresponding Author Secondary Information:	
Corresponding Author's Institution:	University of Bristol School of Earth Sciences
Corresponding Author's Secondary Institution:	
First Author:	Gilles Seropian
First Author Secondary Information:	
Order of Authors:	Gilles Seropian
	John Stix
Order of Authors Secondary Information:	
Manuscript Region of Origin:	CANADA
Abstract:	Caldera collapse events can be sudden and violent in the case of large explosive volcanic eruptions or incremental in the case of long-lived eruptions. Faults nucleating during collapse are associated with seismic activity, but can also host potential economic resources. Yet the kinematic behavior of newly formed faults is poorly constrained. We conducted a series of novel sandbox experiments using piezoelectric sensors to monitor stress perturbations during a caldera collapse. We found excellent spatial and temporal correlations among (a) fault nucleation, inferred from the stress sensor data, (b) the appearance of faults on the surface, and (c) final fault structure, obtained via cross-sections. We estimated fault propagation rates for early inner faults and found that these rates increase with increasing magma evacuation rates. We applied our experimental results to seismic data from natural caldera-forming episodes in order to estimate rates of fault propagation for these systems. Our experiments are consistent with en masse caldera collapse events, such as at Katmai in 1912 and Pinatubo in 1991.
Response to Reviewers:	

Publisher: GSA
Journal: GEOL: Geology
DOI:10.1130/G39551.1

Monitoring and forecasting fault development at actively forming calderas: An experimental study

Gilles Seropian* and John Stix

Department of Earth and Planetary Sciences, McGill University, 3450 University Street, Montreal, Quebec H3A 0E8, Canada

*Current address: School of Earth Sciences, University of Bristol, Wills Memorial Building, Queens Road, Bristol BS8 1RJ, UK

ABSTRACT

Caldera collapse events can be sudden and violent in the case of large explosive volcanic eruptions or incremental in the case of long-lived eruptions. Faults nucleating during collapse are associated with seismic activity, yet the kinematic behavior of newly formed faults is poorly constrained. We conducted a series of novel sandbox experiments using piezoelectric sensors to monitor stress perturbations during a caldera collapse. We found excellent spatial and temporal correlations among (a) fault nucleation, inferred from the stress sensor data, (b) the appearance of faults on the surface, and (c) final fault structure, obtained via cross sections. We estimated fault propagation rates for early inner faults and found that these rates increase with increasing magma evacuation rates. We applied our experimental results to seismic data from natural caldera-forming episodes in order to estimate rates of fault propagation for these systems. Our experiments are consistent with en masse caldera collapse events, such as at Katmai in 1912 and Pinatubo in 1991.

INTRODUCTION

Calderas are large depressions found in all types of volcanic settings. A caldera-forming eruption involves significant hazards on local, regional, and global scales, hence the importance to study and understand the mechanics of such events. Faults forming during caldera collapses play a fundamental role as they control the locations of the eruptive vents, as well as the nature and rate of caldera subsidence.

Notable advances in our knowledge of caldera formation have occurred in the past few decades, thanks to field (e.g., Geshi et al., 2002), experimental (e.g., Roche et al., 2000), theoretical (e.g., Roche and Druitt, 2001) and integrated studies (e.g., Stix and Kobayashi, 2008). Nevertheless, a number of fundamental problems have yet to be solved. When do faults nucleate at depth and how fast do they propagate? How is seismic energy released from the caldera in a spatial and temporal sense?

We address these questions through a series of novel analogue experiments, focusing on the effect of evacuation rate on the kinematics of collapse. We instrumented our experiments with a series of sensors designed to record fault development as a function of both time and space. We then compare our results to historical caldera-forming events.

METHODOLOGY

Experimental Apparatus

Our experimental setup is composed of a 1-m diameter, 1.4-m high cylindrical tank filled with brown sand. We used a water-filled rubber bladder to represent the magma chamber. Once inflated, the bladder is an oblate ellipsoid 30 cm wide and 15 cm thick at the center, with an initial volume of 5 L. The bladder was buried so that its top was ~7 cm beneath the surface, thus yielding a roof aspect ratio (roof thickness / bladder diameter) of 0.23. These conditions represent a natural magma chamber whose roof lies at ~2 km below the surface. Full details of the experimental setup can be found in the Supplemental Material and in Coumans and Stix (2016).

We used piezoelectric sensors to monitor changes in the interior of our sandbox. The sensors feature piezoelectric transducers, which produce an electric signal in response to differential stresses. Thus, our sensors record stress variations. Three sensors were placed on a horizontal line and buried about halfway between the top of the bladder and the surface. The first sensor was located directly above the center of the bladder and the other two were placed above the edge of the bladder. We refer to them as center, east and west sensors, respectively.

In running an experiment, water was pumped out of the bladder, simulating an eruption and triggering the caldera collapse. The evacuation rate was controlled so that, regardless of the duration of the experiment, the final volume of water evacuated from the bladder was 50% of the initial volume. After each experiment, we sectioned the caldera to obtain pictures of cross sections.

Scaling Relations

Every parameter of the experiment was carefully scaled to accurately reproduce natural caldera collapses (Sanford, 1959). For each fundamental dimension X, we define a ratio $X^* = X_{\mathrm{model}} / X_{\mathrm{nature}}$. Our length ratio is $L^* = 3.5 \times 10^{-5}$, so that our 35 cm calderas represent a 10 km diameter caldera in nature. Gravitational conditions are identical in nature and in our model, thus $g^* = L^* T^{*-2} = 1$, yielding a time scaling ratio of $T^* = (L^*)^{½}$ $= 5.9 \times 10^{-3}$. Dry sand has a bulk density of 1650 kg m^{-3} whereas the density of volcanic rocks is ~2800 kg m^{-3}. Hence our density ratio is $\rho^* = 0.59$. The density ratio for the fluids (water with density of 1000 kg m^{-3} and magma with density of 2200 kg m^{-3}) is 0.45, which is within the same order of magnitude. The stress ratio is $\sigma^* = \rho^* g^* L^* = 2 \times 10^{-5}$. The natural cohesion of volcanic rocks is ~10^7 Pa (Hoek et al., 1995) but can be as low as 10^6 Pa (Schultz, 1996). It is difficult to precisely determine our sand cohesion, but it is safe to assume it is within 0–100 Pa, which is reasonable for our purpose. Finally the viscosity ratio is given by $\mu^* = \sigma^* T^* \approx 10^{-7}$. Since $\mu_{water} = 10^{-3}$ Pa s, this represents a natural magma with a viscosity of 10^4 Pa s.

Limitations

We focus solely on fault nucleation and propagation as the caldera develops, so our experiments did not include any pre-existing structural discontinuities, although they are present in nature because of magma chamber inflation or local tectonics. Furthermore, our experiments did not include any temperature, magma rheology, ring dikes or vent-migration effects, which can influence the collapse dynamics (e.g., Kennedy et al., 2008). However, our simplified approach allows us to focus on and isolate the caldera response to evacuation of the magma chamber. The stress changes recorded by the piezometers are not directly equivalent to ground motion recorded by seismometers at real calderas. Nevertheless, they provide a good approximation and guide to the locations of seismic events in nature. Lastly, our magma evacuation procedure did not include eruption and accumulation of material at the surface. Although such processes are likely to influence caldera subsidence, our procedure focuses directly upon how the roof of the reservoir responds to progressive evacuation of the reservoir.

RESULTS

Publisher: GSA
Journal: GEOL: Geology
DOI:10.1130/G39551.1

A key objective was to compare fault development for a caldera that formed rapidly at relatively high evacuation rates versus one that formed more slowly at reduced evacuation rates. Hence the duration of our first experiment (A) was 2.5 min with an evacuation rate of 1 L min^{-1}; for the second experiment (B) the duration was 12.5 min with an evacuation rate of 0.2 L min^{-1}.

Both experiments followed the four general stages commonly observed and summarized by Acocella (2007). Deformation starts with broad sagging, before the first inner faults appear. Peripheral regions then start subsiding, and finally, outer faults appear on the surface. The output from the stress sensors is presented in Figure 1 for both experiments; the sensor units are arbitrary. For each experiment, we studied the most significant faults and noted the time at which they appeared on the surface. For experiment A, we picked the first fault appearing, the second inner fault, the eastern outer fault, and the western outer fault. For experiment B, we used the first fault, the western outer fault, and a large northwestern embayment. For both experiments, the first fault was the most obvious and significant feature as it appeared on the surface.

In experiment A, the signals from the three sensors are flat and steady before the experiment starts (Fig. 1A). All three sensors record a large offset as the experiment is initiated by the pump being turned on. The signals return to a flat, steady pattern after a few seconds. The first noticeable event occurs in the center sensor signal; after a few small spikes, a very large drop occurs, starting at 20.5 seconds. The first fault also appears in the central area between 23.5 and 24.5 s (Fig. 2A). This drop is followed by a positive signal peaking at ~33 s and then decaying for ~20 s. A second smaller peak is observed at ~56 s, and the second set of inner faults appear on the surface at 58–59 s. The center sensor signal then becomes flat, with progressively fewer perturbations until the end of the experiment. The east sensor is the next to record a period of unrest. From 75 s until the end of the experiment, the deviations from the baseline signal are much larger, with maximum amplitudes between 85 and 110 s. The eastern outer fault appears between 67 and 70 s. From 125 s until the end of the experiment, the west sensor shows a period of high activity relative to its baseline. This coincides with the appearance of the western outer fault at the surface between 117 and 120 s. Outer faults propagate all around the caldera until ~125 s. After this time, the caldera continues to deepen but ceases its outward growth. All three sensors return to their initial state after the experiment ends at 150 s.

In experiment B, the three sensor signals are flat before the start of the experiment. Large perturbations are observed as the experiment starts. At 55 s, the center sensor signal starts dropping and forms a very large trough with a minimum value at ~80 s. The first fault appears on the surface at 96–98 s. This is followed by a positive signal, which peaks at 170 s, then slowly decays to ~415 s. The noise level is also much higher than beforehand, especially between 120 and 220 s. The west sensor records a period of activity starting at 500 s until the end. Western outer faults first appear between 406 and 410 s and then propagate very slowly. A large embayment appears on the northwestern edge between 491 and 495 s. By ~500 s, the caldera is well defined and stops propagating outward. It deepens, however, and the walls become more defined until the end of the experiment. The east sensor records a few medium amplitude peaks toward the end of the experiment but no large amplitude signal.

The stress field is not spatially uniform during an experiment (Roche et al., 2000). Thus, the polarity of the signal (Fig. 1) is an indicator of whether the sensor is experiencing compressive or tensile stresses.

For experiment A, we show a plan view of the final deformation pattern after the experiment (Fig. 2A) and a representative cross section (Fig. 2B). We use a color code in Figures 1 and 2 to illustrate fault development, in order to show (1) the faults' first appearance on the surface and the respective sensor response (Fig. 1A) and their respective location in the caldera (Fig. 2).

The final surface deformation is complex, with many small faults (Fig. 2A). However, the overall pattern is consistent with the results obtained by Kennedy et al. (2004). Our cross-sectional data (Fig. 2B) are also consistent with observations made by Kennedy et al. (2004). Inner faults are outward dipping whereas outer faults are inward dipping. The set of inner faults is complex with many subsurface branches. The outer faults accommodated significant displacement on both sides and do not exhibit branching.

In summary, there is a clear correlation between stress perturbations, as recorded by our sensors during the course of an experiment, and fault development at the surface. Most notably, the large early trough is followed shortly by the first appearance of the main inner fault at the surface.

FAULT EVOLUTION

Despite the different run times, the two experiments are broadly comparable in terms of fault development and caldera evolution (Fig. 1A and 1B). In both cases, the center sensor was the first to record significant events, namely a very large drop followed by a large peak. The west sensor exhibited very similar signals for both experiments, showing activity and instability near the end. For the east sensor, in experiment B there were very few perturbations compared to experiment A. This may be due to the fact that only a small amount of faulting developed on the eastern side of the caldera in experiment B. The style of collapse is therefore very close.

Fault nucleation processes are intimately related to stress perturbations. Faults are localized, irreversible ruptures. They form as a response to decompression of the magma chamber. Fault nucleation and propagation therefore produce a local, sudden stress drop. Our sensors record stress changes; thus, perturbations from the equilibrium state of the sensors are associated with fault nucleation sequences. This hypothesis is supported by the excellent correlation between (a) periods of large deviations relative to background in the sensor recordings and (b) fault formation observed at the surface. The correlation is spatial as well as temporal; when a fault appears at the surface, it is always the closest sensor that records significant variations. Furthermore, the sensors' response to stress variations decreases rapidly with distance, reinforcing the idea that the largest observed signals from a particular sensor are generated by faults forming closest to that sensor. It is thus possible to follow the stages of collapse from the signals in Figure 1. The collapse is initiated along an inner fault in the central area, consistent with major changes in the center sensors stress signals, while the outer sensors record nothing. The outer faults form asymmetrically; they start nucleating on one side before propagating to the other. This behavior is particularly visible in experiment A for which our visual observations suggest that collapse is initiated on the east side and then propagates to the west. This is again consistent with the data in Figure 1A where the east sensor records high stress changes beginning at ~70 s, while the west sensor does not record any instability until ~110 s.

We observe two distinct faulting patterns in the stress signal (Fig. 1). On one hand, the appearance of inner faults at the surface are preceded by a large, single peak in the sensor signal. By contrast, outer faults are not associated with any stress deviation before they appear on the surface, but they are followed by intense stress fluctuations. These contrasting stress patterns can be explained by distinct fault dynamics.

Inner faults propagate from the top of the magma chamber upward, whereas outer faults nucleate at the surface and propagate downward. This difference has been well documented (e.g., Roche et al., 2000; Kennedy et al., 2004; Acocella, 2007; Burchardt and Walter, 2010). It is confirmed in our experiments by observing how the amount of displacement accommodated by each fault varies with depth (see GSA Data Repository[1]). The direction of propagation therefore explains why inner faults are recorded in the stress signal before they are visible at the surface, while outer faults exhibit stress perturbations only after they nucleate at the surface and propagate downward.

Inner and outer faults also exhibit two distinct growth modes (see the Data Repository). The large and abrupt peaks associated with inner faults suggest a rapid and sudden fault development. By contrast, outer faults produced several smaller peaks in the stress signal for a longer period. This indicates slower, more incremental fault growth.

By indicating when faults nucleate, our sensor data give us insight on where and when earthquakes occur during subsidence. The center sensor records sudden, large stress changes, suggesting en masse caldera collapse at an early stage of caldera evolution. These data resemble those for collapse at Katmai in 1912 and Pinatubo in 1991 (Stix and

Kobayashi, 2008). In these natural collapses, large amounts of seismic energy were suddenly released about halfway through the eruptions. The largest signals we observed are the first very large drops recorded by the center sensor in both experiments. This would thus correspond to the largest seismic events, followed later by smaller magnitude earthquakes, corresponding to events recorded by the east and west sensors. In our experiments, the largest events occur after less than 10% of the reservoir volume is evacuated, as opposed to midway through the climactic eruption sequence as observed at Katmai and Pinatubo. This is due to the different aspect ratios involved (roof thickness/magma chamber diameter). Our experiments had an aspect ratio of 0.23 whereas Katmai and Pinatubo have aspect ratios of 2.0 and 2.4, respectively. At higher aspect ratios, faults form later (Roche et al., 2000), delaying seismic events.

Stix and Kobayashi (2008) showed that this sudden, en masse collapse behavior contrasts strongly with a longer, more continuous style of collapse, as observed at Miyakejima (Japan, Geshi et al., 2002) in 2000, and Bárðarbunga (Iceland, Gudmundsson et al., 2016) in 2014–2015. This latter style of collapse involves (a) basaltic magma as opposed to the more silicic magmas of Katmai and Pinatubo, and (b) slower magma evacuation rates (1.7×10^2 and 1.2×10^2 m^3 s^{-1} for Miyakejima and Bárðarbunga, respectively, compared to 2.2×10^5 and 3.6×10^5 m^3 s^{-1} for Katmai and Pinatubo, respectively). The end result is a protracted and progressive style of collapse. Future experimental work could easily model this behavior and examine detailed stress perturbations under these conditions.

FAULT PROPAGATION

By focusing on the timing of both the first sharp drop in the sensor signal and the associated fault's appearance at the surface, we can estimate the rate of fault propagation from the magma chamber to the surface. First, we measure the time delay Δt between the beginning of the drop in the sensor signal and the fault's appearance at the surface. Inner faults nucleate on top of the magma chamber and propagate upward. Knowing the depth of the top of the magma chamber h, we can then compute the model propagation rate $R_{model} = h/\Delta t$, which is 0.023 ± 0.005 m s^{-1} for experiment A and 0.00168 ± 0.00004 m s^{-1} for experiment B. We then scale back to natural speeds using $R_{nature} = R_{model}/R^*$, where R^* is the propagation rate scaling ratio given by $R^* = L^*T^{*-1}$. This scaling up produces fault propagation rates for natural systems of 3.8 m s^{-1}, based on experiment A, and 0.28 m s^{-1}, based on experiment B. A higher evacuation rate therefore yields a higher fault propagation rate.

We can now apply these propagation rates to natural settings at Katmai and Pinatubo and compare our estimates to real seismic data. Propagation rates depend on evacuation rates, hence, to choose the appropriate propagation rate for natural systems, we scale our experimental evacuation rates E_{model} back to natural values E_{nature} using $E_{nature} = E_{model}/E^*$ and the scaling ratio $E^* = L^{*3}T^{*-1}$ (see Scaling Relations section). Values for E_{nature} are 2.3×10^6 m^3 s^{-1} and 4.6×10^5 m^3 s^{-1} based respectively on experiments A and B. The value from experiment B is similar to observed evacuation rates at Katmai and Pinatubo ($2.2–3.6 \times 10^5$ m^3 s^{-1}). Hence we apply a fault propagation rate of 0.28 m s^{-1} to natural systems.

In the case of Katmai, the top of the magma chamber was 4–5 km beneath the surface (Hildreth and Fierstein, 2000). Based on this depth and our chosen fault propagation rate of 0.28 m s^{-1}, we obtain a time interval of 238–298 min for faults nucleating at the top of the magma chamber to reach the surface. This timescale can be compared with the occurrence of earthquakes at Katmai. The largest earthquakes occurred on 8 June 1912 between 0611 and 1300 h UTC, representing an elapsed time of 409 min. This interval is comparable to our experimental data and scaling analysis, suggesting that the major caldera-forming fault system at Katmai was established and complete, from the top of the magma chamber to the surface, within 6.8 h, resulting in caldera subsidence.

For Mount Pinatubo, the top of the magma chamber was ~6 km deep (Mori et al., 1996). According to our analysis, it would then take 357 min for a fault to propagate all the way to the surface. During the climactic eruption on 15 June 1991, the largest seismic events of M5 and greater occurred from 0739 to 1225 h UTC, yielding a total elapsed time of 286 min. However, the bulk of seismic energy was released over a comparatively short interval of 51 min stretching from 1041 to 1132 UTC. This observation suggests that both the fault propagation rate and magma evacuation rate were unusually high during this time. This is not surprising, since the evacuation rate likely undergoes substantial variations during such eruptions. Despite the aspect ratio difference, the elevated evacuation rates in our experiments and for our natural examples (Katmai and Pinatubo) indicate a specific sequence of fault growth. The principal inner faults, which form rapidly, contrast with the longer durations and timescales of the outer faults. This dichotomy may be explained as a drawn-out response of the outer faults to sudden, large-scale fault movement in the central region of the caldera. Furthermore, significant seismicity may occur under certain conditions after the climactic eruption. In our experiments, all stress perturbations and faulting ceased when the pump was turned off. In nature, however, some further magma evacuation may be expected to occur after the large eruption from a series of smaller eruptions, subsurface magma drainage, or both. A certain threshold may be reached, which causes further subsidence and associated earthquakes. This was observed at both Katmai and Pinatubo.

CONCLUDING REMARKS

Using piezoelectric sensors in a series of analogue caldera collapse experiments we were able to document stress perturbations of en masse caldera collapses similar to natural events such as at Katmai in 1912 and Pinatubo in 1991. Our results provide insight on the timing, location, and evolution of fault nucleation. This new and original experimental technique may be used to model other kinematic behaviors. We also estimated the propagation rate of early inner faults. This type of information is essential for our understanding of seismicity and fault development during caldera formation and, ultimately, our ability to assess and mitigate hazards in such settings.

ACKNOWLEDGMENTS

We thank Joan Martí, Nobuo Geshi, Valerio Acocella, and an anonymous reviewer for their constructive comments. We would also like to thank Jason Coumans for his help in setting up these experiments. This work was funded by Discovery and Accelerator grants to JS from the Natural Sciences and Engineering Research Council of Canada.

REFERENCES CITED

Acocella, V., 2007, Understanding caldera structure and development: An overview of analogue models compared to natural calderas: Earth-Science Reviews, v. 85, p. 125–160, https://doi.org/10.1016/j.earscirev.2007.08.004.

Burchardt, S., and Walter, T.R., 2010, Propagation, linkage, and interaction of caldera ring-faults: Comparison between analogue experiments and caldera collapse at Miyakejima, Japan, in 2000: Bulletin of Volcanology, v. 72, p. 297–308, https://doi.org/10.1007/s00445-009-0321-7.

Coumans, J.P., and Stix, J., 2016, Caldera collapse at near-ridge seamounts: An experimental investigation: Bulletin of Volcanology, v. 78, p. 70–89, https://doi.org/10.1007/s00445-016-1065-9.

Geshi, N., Shimano, T., Chiba, T., and Nakada, S., 2002, Caldera collapse during the 2000 eruption of Miyakejima Volcano, Japan: Bulletin of Volcanology, v. 64, p. 55–68, https://doi.org/10.1007/s00445-001-0184-z.

Gudmundsson, M.T., et al., 2016, Gradual caldera collapse at Bárdarbunga volcano, Iceland, regulated by lateral magma outflow: Science, v. 353, no. 6296, https://doi.org/10.1126/science.aaf8988.

Hildreth, W., and Fierstein, J., 2000, Katmai volcanic cluster and the great eruption of 1912: Geological Society of America Bulletin, v. 112, p. 1594–1620, https://doi.org/10.1130/0016-7606(2000)112<1594:KVCATG>2.0.CO;2.

Hoek, E., Kaiser, P.K., and Bawden, W.F., 1995, Support of underground excavations in hard rock: Rotterdam, Netherlands, A.A. Balkema, 215 p.

Kennedy, B., Stix, J., Vallance, J.W., Lavallée, Y., and Longpré, M.-A., 2004, Controls on caldera structure: Results from analogue sandbox modeling: Geological Society of America Bulletin, v. 116, p. 515–524, https://doi.org/10.1130/B25228.1.

Kennedy, B.M., Jellinek, A.M., and Stix, J., 2008, Coupled caldera subsidence and stirring inferred from analogue models: Nature Geoscience, v. 1, p. 385–389, https://doi.org/10.1038/ngeo206.

Mori, J., Eberhart-Phillips, D., and Harlow, D.H., 1996, Three-dimensional velocity structure at Mount Pinatubo: Resolving magma bodies and earthquake hypocenters, *in* Newhall, C.G., and Punongbayan, R.S., eds., Fire and Mud: Eruptions and Lahars of Mount Pinatubo, Philippines: Quezon City, Philippines, Philippine Institute of Volcanology and Seismology, and Seattle, Washington, University of Washington Press, p. 371–382.

Roche, O., and Druitt, T.H., 2001, Onset of caldera collapse during ignimbrite eruptions: Earth and Planetary Science Letters, v. 191, p. 191–202, https://doi.org/10.1016/S0012-821X(01)00428-9.

Roche, O., Druitt, T.H., and Merle, O., 2000, Experimental study of caldera formation: Journal of Geophysical Research: Solid Earth, v. 105, p. 395–416, https://doi.org/10.1029/1999JB900298.

Sanford, A.R., 1959, Analytical and experimental study of simple geologic structures: Geological Society of America Bulletin, v. 70, p. 19–52, https://doi.org/10.1130/0016-7606(1959)70[19:AAESOS]2.0.CO;2.

Schultz, R.A., 1996, Relative scale and the strength and deformability of rock masses: Journal of Structural Geology, v. 18, p. 1139–1149, https://doi.org/10.1016/0191-8141(96)00045-4.

Stix, J., and Kobayashi, T., 2008, Magma dynamics and collapse mechanisms during four historic caldera-forming events: Journal of Geophysical Research, v. 113, B09205, https://doi.org/10.1029/2007JB005073.

FIGURE CAPTIONS

Figure 1. Stress evolution during (A) experiment A and (B) experiment B. The times at which faults of interest appear on the surface are indicated.

Figure 2. A: Final surface deformation of experiment A, viewed from above with lighting from the west. Faults are highlighted. B: Cross section of experiment A. The plane of view is indicated in A. Faults are highlighted. The former surface of the experiment is shown in red.

1GSA Data Repository item 2017xxx, **[[Please provide item names and brief description here]]**, is available online at http://www.geosociety.org/datarepository/2017/ or on request from editing@geosociety.org.

Figure 1 Click here to download Figure Figure1.pdf

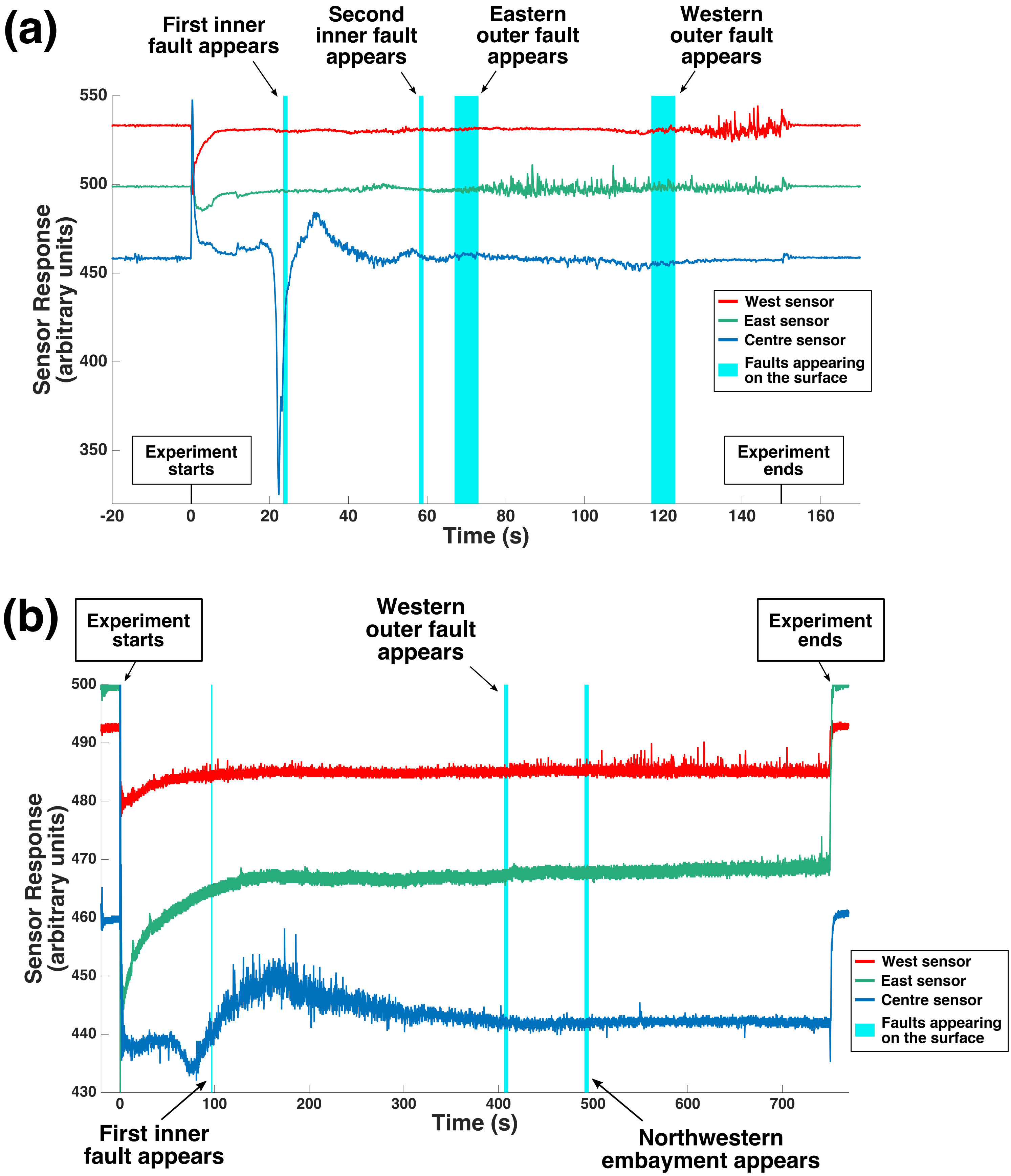

Figure 2 Click here to download Figure Figure2.pdf

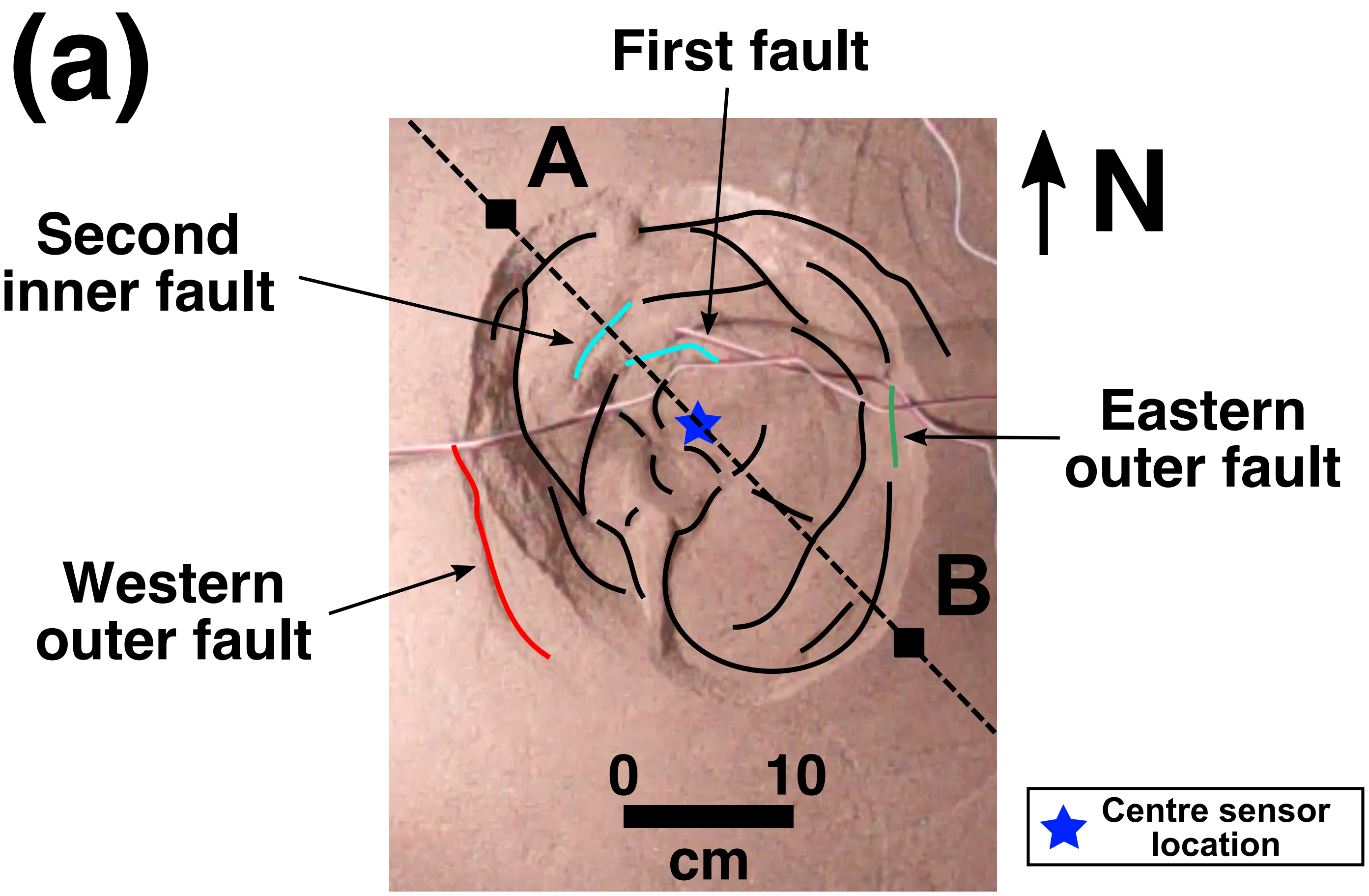

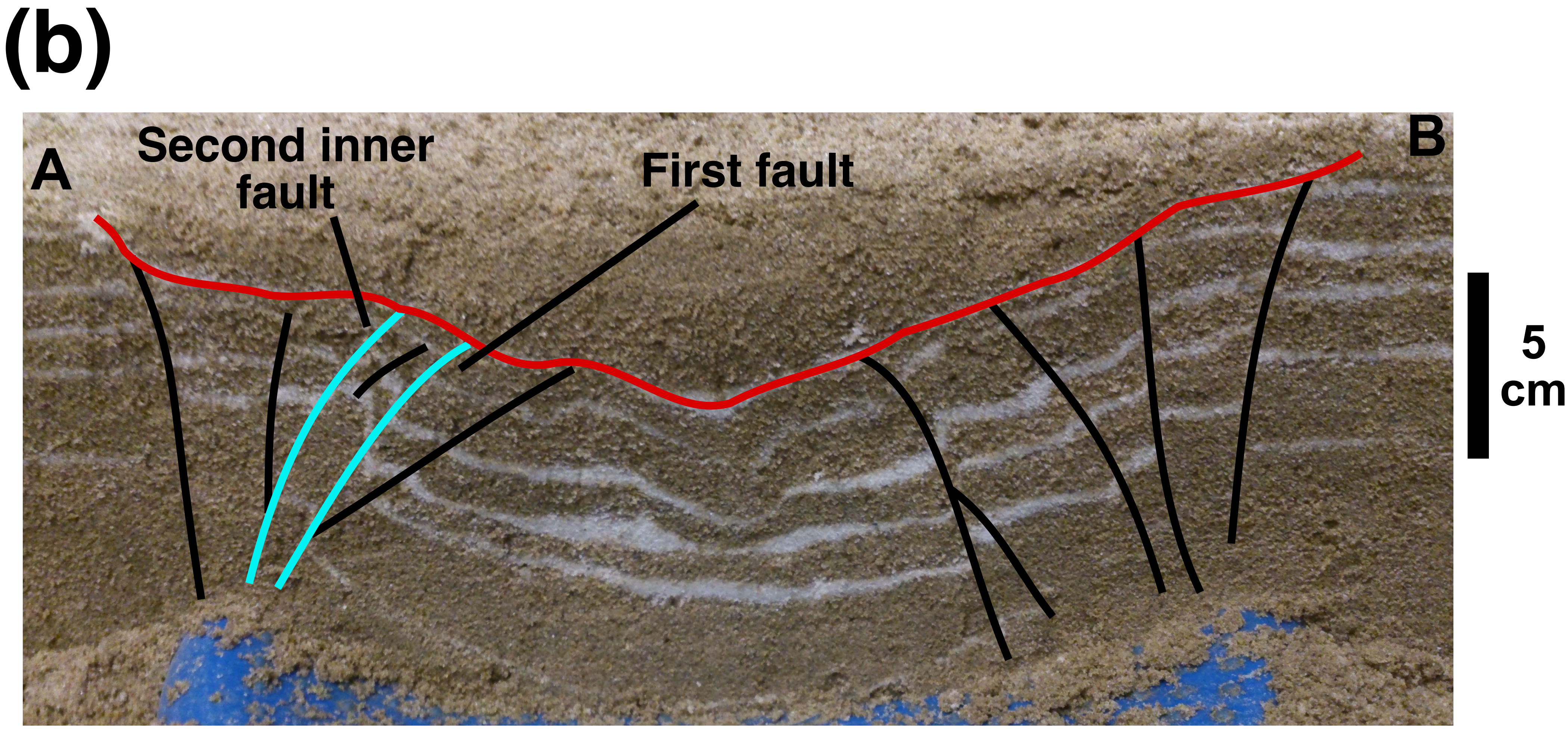

SUPPLEMENTARY MATERIAL

EXPERIMENTAL SETUP

The experimental apparatus consists of a large cylindrical tank, with a diameter of 1 m and a height of 1.4 m (Figure S1a). The tank is filled with brown sand. A water-filled bladder is placed in the center of the tank and carefully levelled. It is connected to a pump via a hose going downward, through a hole at the bottom of the tank. We add brown sand until only the top of the bladder is exposed. From this point, we add brown sand layer by layer. Each layer is about 1 cm thick. We compact each layer with a wooden board to limit pore space and increase sand cohesion. A thin layer of white industrial quartz (sandblasting sand) is added between each layer of brown sand as a colour marker; this serves to trace faults after the experiment.

The electronic sensors are carefully placed between two layers of brown sand, halfway between the top of the magma chamber and the surface at a depth of 3.5 cm (Figure S2b). Cables connecting the sensors are carefully levelled and taped to the edge of the tank to avoid disturbing faulting processes. The sensors are arranged in a line (Figure S2) and labelled "east", center" and "west", respectively.

PIEZOELECTRIC SENSORS

We used piezoelectric sensors to monitor our apparatus (Figure S1b). The sensors are produced by Phidgets Inc. (Phidgets 1104_0 – Vibration sensors). Each sensor features a piezoelectric transducer, which transforms mechanical strain into an electric signal. This analog input is then transmitted to a computer through an analog-to-digital converter (Phidgets 1018_2 - PhidgetInterfaceKit 8/8/8) with a sampling frequency of 49 Hz. Hence, we obtain a time series of the local stress state around each sensor.

The sensitivity of the sensors falls off steeply with distance. The sensors generally record changes occurring within a radius of ~2 cm, although this value depends on the amplitude of the event considered.

The values outputted by the sensors are not calibrated, in the sense that it is impossible to relate these values to real stresses. This is why the time series are presented with arbitrary units (a.u.). However, all sensors are calibrated with respect to each other; for instance, a change of 20 a.u. in the centre sensor data is equivalent to a change of 20 a.u. in the west centre. The calibration also holds between different experiments, i.e., the values recorded in experiment A can be compared directly to those from experiment B.

DATA ANALYSIS

Spectrograms

Figure S3 and S4 show spectrograms associated with each sensor signal for experiment A and B, respectively. Each spectrogram presents the time evolution of the frequency power spectrum. The spectrograms are computed via the short-time Fourier Transform of a moving window, containing 130 data points for experiment A (i.e. 2.6 seconds) and 400 data points for experiment B (i.e. 8.2 seconds). All spectrograms corroborate the observations of the stress signal given in the main text.

In experiment A, the frequency spectrum of all sensors is steady and restricted to low frequencies (<3 Hz, Figure S3) during the first twenty seconds. The first significant change occurs in the centre sensor signal at about 20 seconds. Here, there is a sudden increase in the range of frequencies (0-25 Hz). There is also an important increase in the intensity of lower frequencies. This is followed by a rapid decrease of the frequency range (0-15 Hz at 27 seconds). The frequency range then steadily decays back until the end of the experiment. This first event corresponds to the first very large drop observed in the stress signal, which we identify to be related to the formation of the first inner faults. The east and west spectrograms stay steady until about 70 and 120 seconds, respectively. At 70 seconds, the east spectrogram features a gradual increase in the range of frequencies, as well as a slight increase of the lower frequencies' intensity. The period of high frequency range is sustained for a longer period than for the centre sensor. The east sensor frequency range then slowly decreases to 0-8 Hz, i.e., above background level, before the experiment is terminated. At 120 seconds, the west spectrogram displays a similar pattern, i.e., a gradual increase in frequency range and a slight increase of the lower frequencies' power. The experiment ends while the frequency range of the west sensor signal is still high. For both the east and west sensors, the aforementioned spectrogram features happen at similar times as fault nucleate at the surface.

Concerning experiment B (Figure S4), the background level comprises frequencies between 0-3 Hz. The first significant deviations from background occur in the centre spectrogram at about 75 seconds. Here, we see a sudden increase in the range of frequencies (0-17 Hz). This increases steadily to a maximum 0-24.5 Hz around 180 seconds (i.e., the maximum frequency our sensors can record). It then steeply decays back to background level, where it stays until the end of the experiment. The west spectrogram displays some interesting features starting at 500 seconds. The frequency range increases to 0-10 Hz. It then fluctuates between 0-5 Hz and 0-10 Hz until the experiment is terminated. Finally, the east spectrogram does not display much perturbation from background level, although a slight increase in frequency range occurs during the last minute of the experiment. The patterns observed in these three spectrograms are in agreement with the analysis of the stress signals. The timing of the large variations observed in the range of frequencies concurs very well with visual observations of faults forming at the surface.

Our frequency spectrum analysis of the sensor stress signal supports our hypothesis that structures observed in the stress output can be related to faulting processes. In term of frequencies, fault nucleation involves an increase in frequency range and power.

Inner faults vs. outer faults

We present close-up views of the important features from Figure 1 in the main text. Figure S5 focuses on experiment A whereas Figure S6 is concerned with experiment B.

Figure S5 presents the stress data from (a) the centre sensor when the first fault appears, (b) the east sensor when the eastern outer fault appears and (c) the west sensor when the western fault appears. The stress signals are very different between the first inner fault (a) on one hand and the outer faults (b and c) on the other hand. The signal from the centre sensor in Figure S5a features a large, abrupt drop, reaching a minimum two seconds before the first fault appears at the surface. The signals in Figure S5b and S5c are qualitatively and quantitatively similar. There is no deviation from the background signal before the outer faults appear. Once the faults are observed on the surface, the signal peak-to-peak amplitude gradually increases from ~5 a.u. to ~20 a.u. The duration of the event recorded by the east sensor signal is longer than the one from the west sensor; this is because the experiment was manually stopped after 150 s, putting an end to faulting activity. The stress output therefore strongly contrasts between inner and outer faults.

It is worth noting that this dichotomy can also be observed in the spectrograms (Figure S3). The centre sensor displays a sharper increase and a more rapid decrease in frequency range, as well as higher intensity for lower frequencies. On the other hand, the east and west sensors exhibit more gradual and less powerful but more sustained spectrograms.

The trends observed in experiment B are similar to the trends in experiment A. Figure S6 contains the stress evolution from (a) the centre sensor while the first fault appears and (b) the west sensor when the western outer fault appears. The signal in Figure S6a resembles the signal in Figure S5a. It is characterized by a sharp drop, preceding the appearance of the first fault by 17 s. The amplitude of the deviations increases after this first drop. We can then observe a positive peak, followed by a slow decrease back to background level. Similarly, Figure S6b is comparable to Figure S5b and S5c, though less striking. The stress pattern shows no deviation before the outer fault appears but features a gradual increase in peak-to-peak amplitude, from 2 a.u. to 15 a.u., once the fault has appeared on the surface. As for experiment A, the differences observed between inner and outer fault in the stress signal are also visible in the spectrograms (Figure S4).

DIRECTION OF FAULT PROPAGATION

Here, we support our claim that outer faults propagate downwards whereas inner faults propagate upwards. We present results for one outer fault and one inner fault; however, the analysis holds for all faults.

We focus on the left-hand side of the cross section from Figure 2B in the main text. Using the white sand markers, we can measure the displacement accommodated by the fault at three different depths: close to the surface, close to the magma chamber, and halfway in between. We highlight the white sand markers on each side of the fault, using a color code (Figure S7). The displacement on the fault is indicated at each depth. The outer fault displays progressively less displacement with depth, indicating downward propagation. By contrast, the inner fault accommodated more displacement at depth, suggesting an upward propagation.

FIGURE CAPTIONS

Figure S1: (a) Diagram of the experimental setup. A 1 m diameter cylinder is filled with dry sand. A rubber bladder, filled with water, is buried and connected to a pump. A flowmeter is used to control the flow out of the bladder. A camera is set up above the cylinder to record surface deformation. Sensors are placed halfway between the bladder and the surface. Sensor input is recorded on a computer through an analog to digital converter. (b) A piezoelectric sensor, from Phidgets Inc.

Figure S2: (a) Location of the three sensors during our experiments, viewed from above. (b) The sensors being placed during the preparation of an experiment.

Figure S3: Spectrograms from experiment A. The stress signal from each sensor is presented on top. The cyan rectangles represent periods of fault nucleation at the surface (see main text). The bottom graphs are spectrograms, representing the time evolution of the frequency power spectrum.

Figure S4: Spectrograms from experiment B. The stress signal from each sensor is presented on top. The cyan rectangles represent periods of fault nucleation at the surface (see main text). The bottom graphs are spectrograms, representing the time evolution of the frequency power spectrum.

Figure S5: Stress evolution during experiment A. Fault appearance is indicated by cyan rectangles. (a) Centre sensor when the first fault appears. (b) East sensor when the eastern outer fault appears. (c) West sensor when the western outer fault appears.

Figure S6: Stress evolution during experiment B. Fault appearance is indicated by cyan rectangles. (a) Centre sensor when the first fault appears. (b) West sensor when the eastern outer fault appears.

Figure S7: Cross section of experiment A. One outer fault (left) and one inner fault (right) are highlighted. White sand markers are also highlighted to show fault displacement. Fault displacement is measured using graphics software and indicated next to the corresponding arrow.

Figure S1

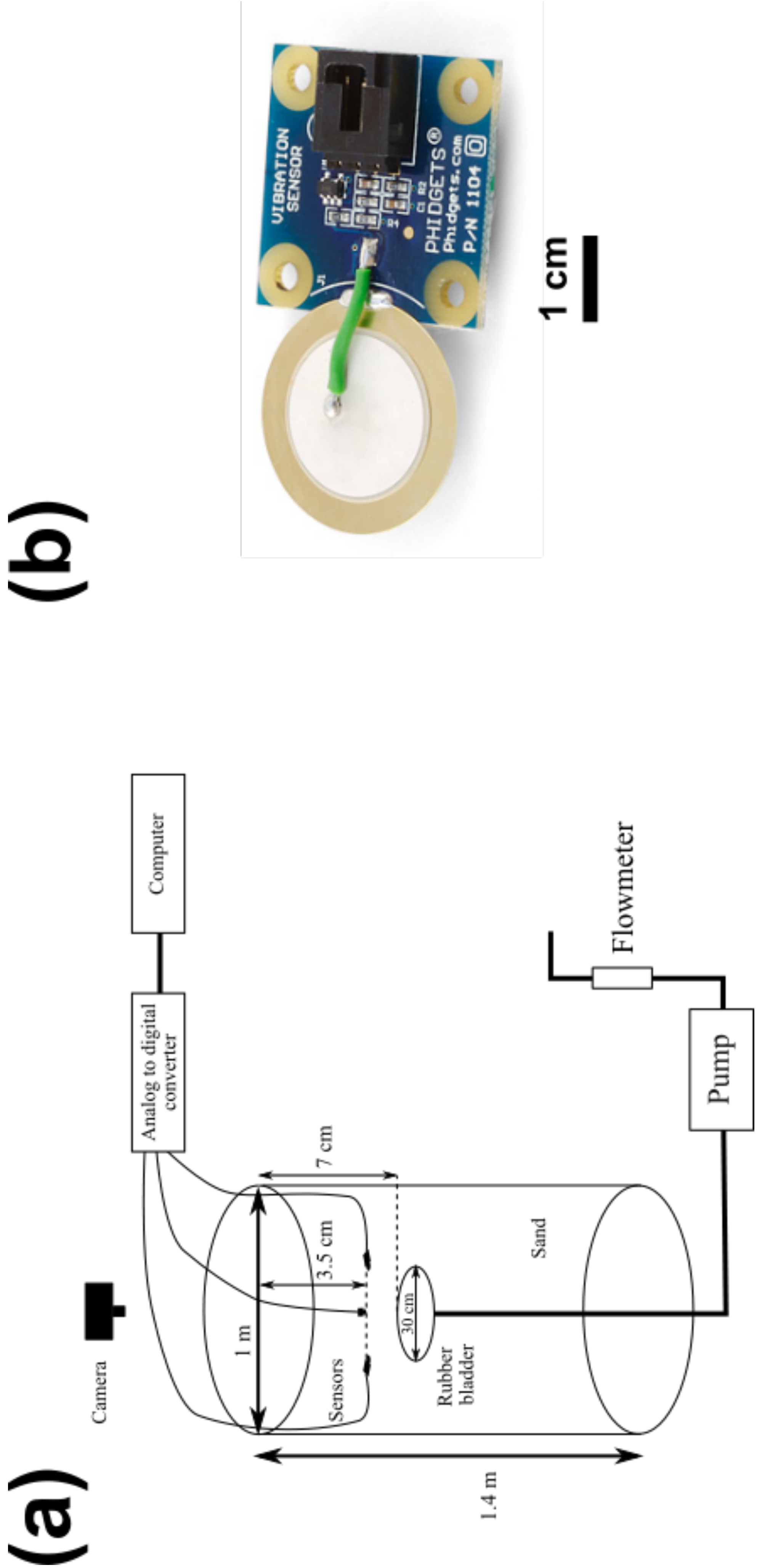
(a)
Camera
Computer
Analog to digital converter
7 cm
3.5 cm
Sand
30 cm
Rubber bladder
Sensors
1 m
1.4 m
Flowmeter
Pump
(b)
VIBRATION SENSOR
PHIDGETS®
Phidgets.com
P/N 1104
1 cm

Figure S2

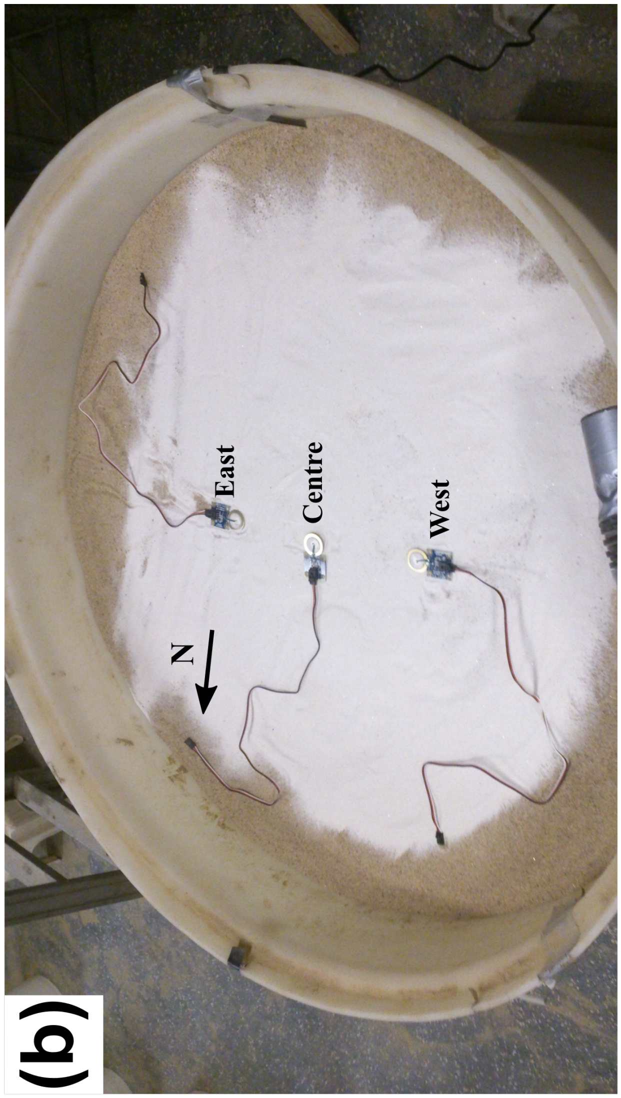

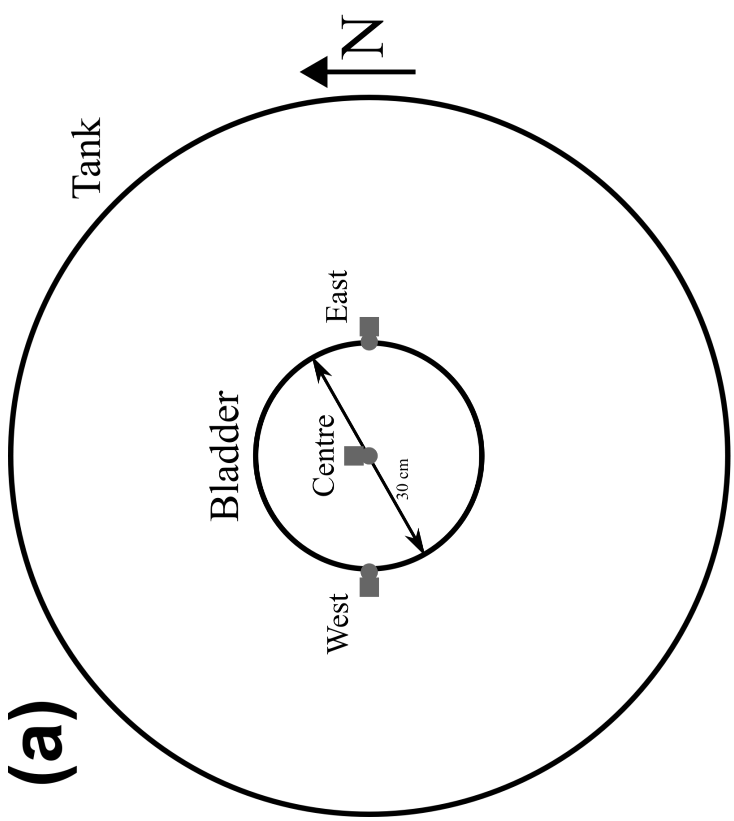

Figure S3

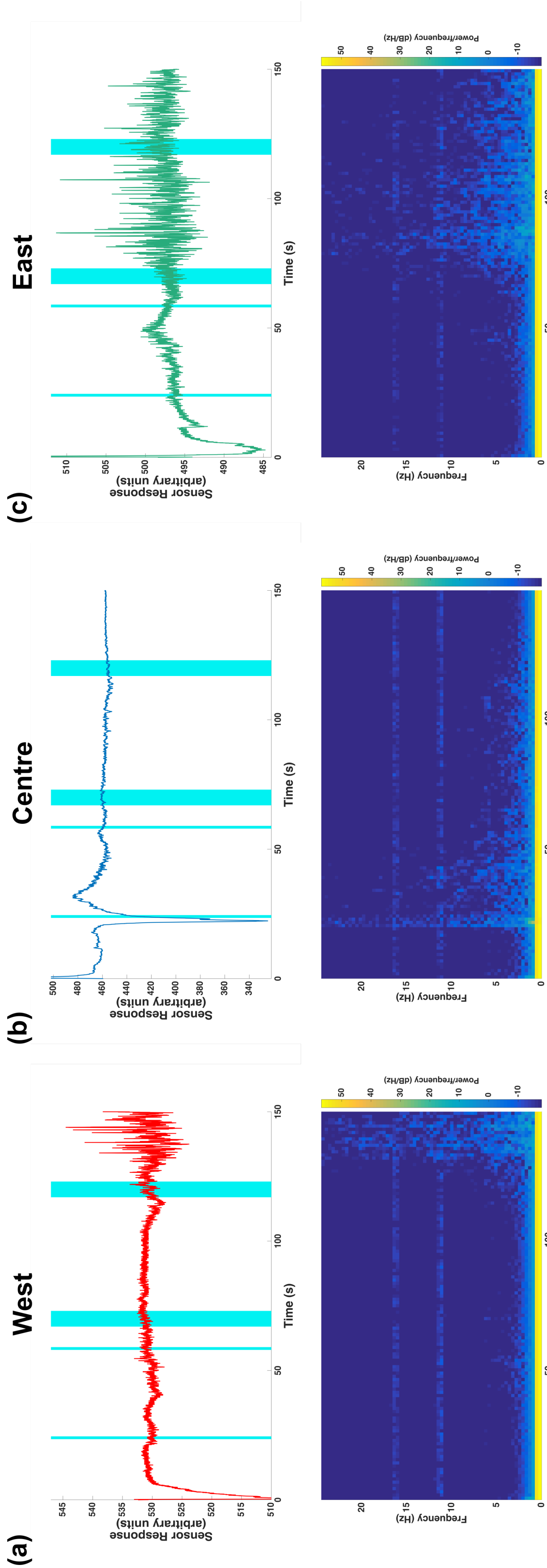
(a)
West
(b)
Centre
(c)
East
Sensor Response (arbitrary units)
Time (s)
Frequency (Hz)
Power/frequency (dB/Hz)

Figure S4

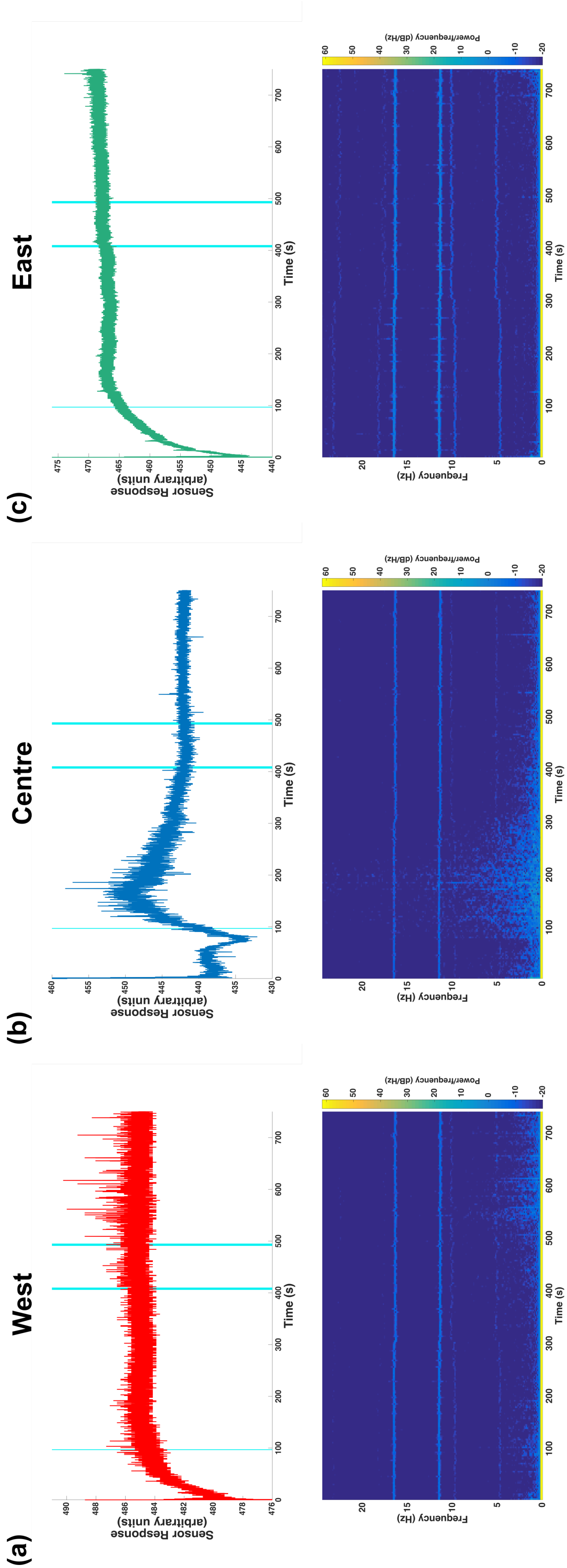

(a)
West
(b)
Centre
(c)
East
Sensor Response (arbitrary units)
Time (s)
Frequency (Hz)
Power/frequency (dB/Hz)

Figure S5

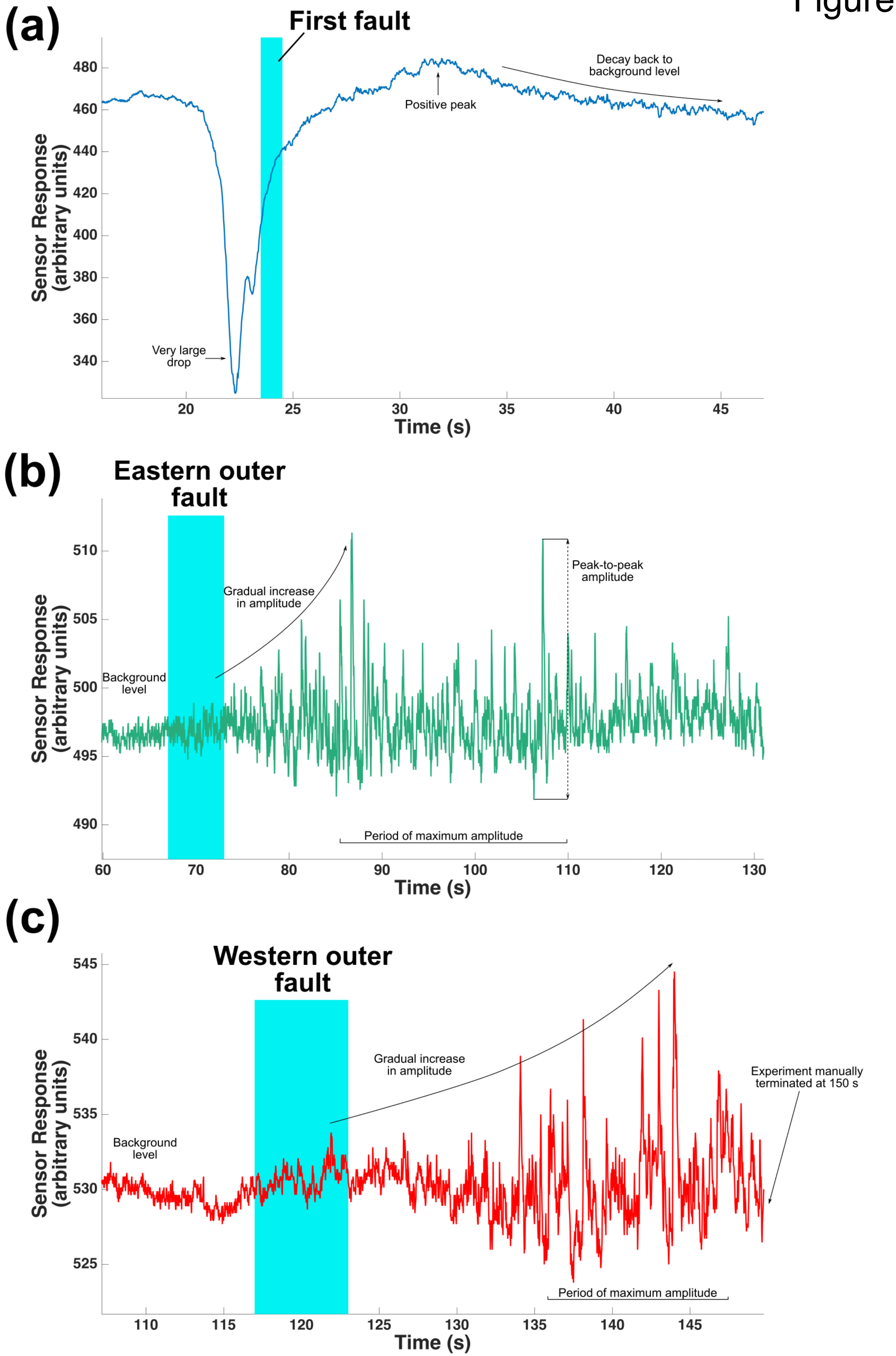

(a)
First fault
Sensor Response (arbitrary units)
480
460
440
420
400
380
360
340
20
25
30
35
40
45
Time (s)
Very large drop
Positive peak
Decay back to background level
(b)
Eastern outer fault
Sensor Response (arbitrary units)
510
505
500
495
490
60
70
80
90
100
110
120
130
Time (s)
Background level
Gradual increase in amplitude
Peak-to-peak amplitude
Period of maximum amplitude
(c)
Western outer fault
Sensor Response (arbitrary units)
545
540
535
530
525
110
115
120
125
130
135
140
145
Time (s)
Background level
Gradual increase in amplitude
Experiment manually terminated at 150 s
Period of maximum amplitude

Figure S6

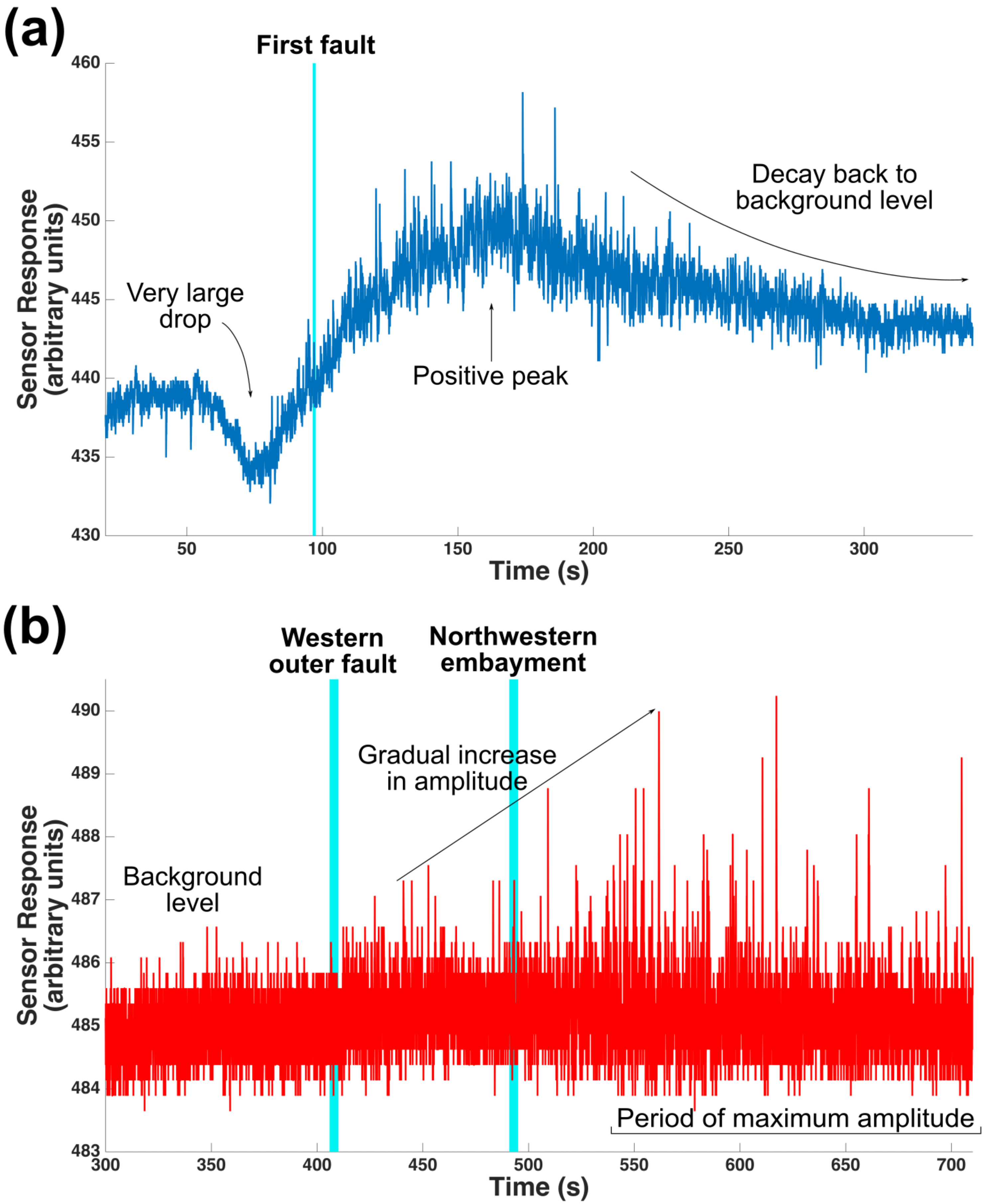
(a)
First fault
Very large drop
Positive peak
Decay back to background level
Sensor Response (arbitrary units)
Time (s)
460
455
450
445
440
435
430
50
100
150
200
250
300
(b)
Western outer fault
Northwestern embayment
Gradual increase in amplitude
Background level
Period of maximum amplitude
Sensor Response (arbitrary units)
Time (s)
490
489
488
487
486
485
484
483
300
350
400
450
500
550
600
650
700

Figure S7

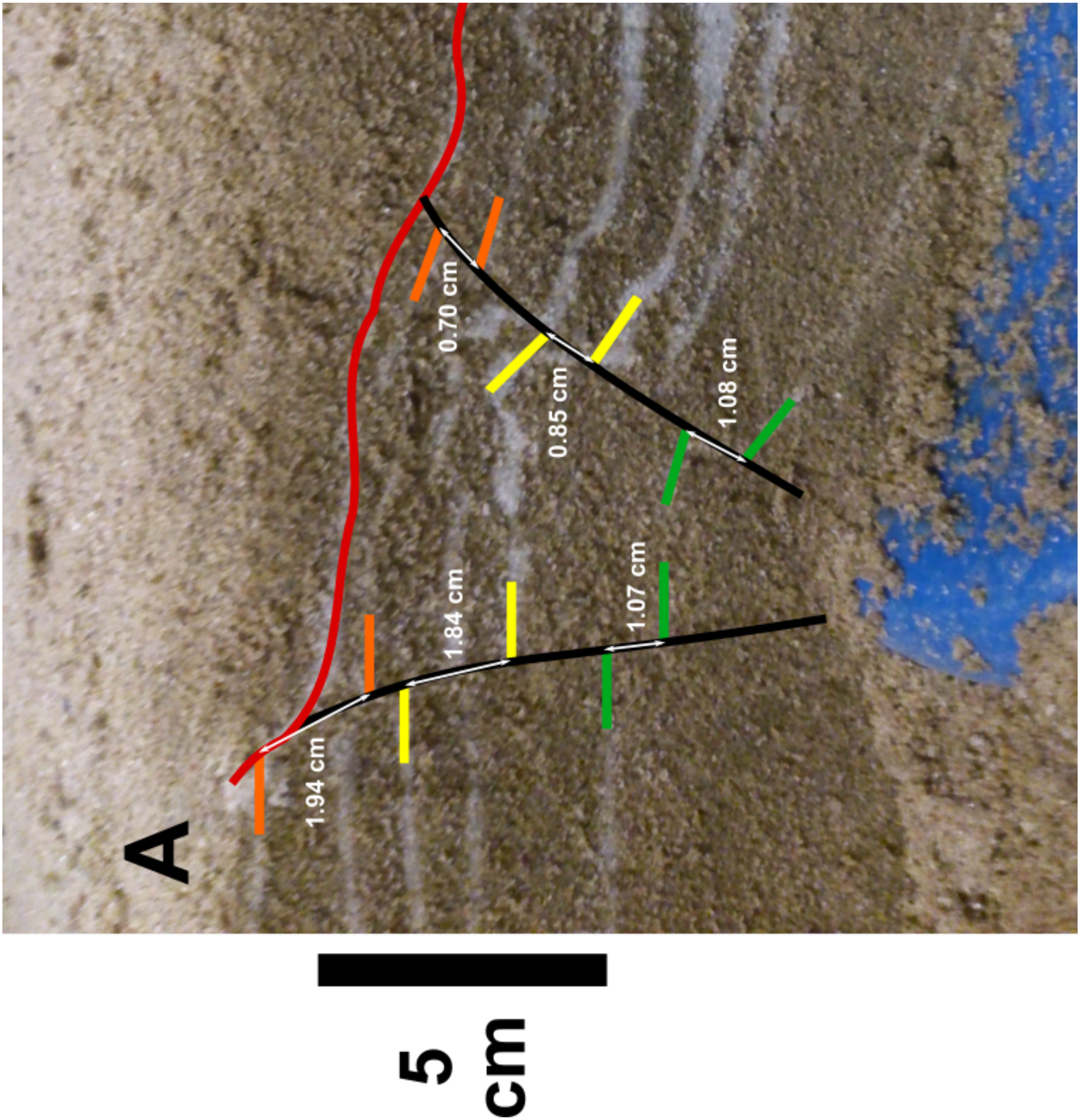

Publisher: GSA
Journal: GEOL: Geology
DOI:10.1130/G39551.1

Monitoring and forecasting fault development at actively forming calderas: An experimental study

Gilles Seropian* and John Stix

Department of Earth and Planetary Sciences, McGill University, 3450 University Street, Montreal, Quebec H3A 0E8, Canada

*Current address: School of Earth Sciences, University of Bristol, Wills Memorial Building, Queens Road, Bristol BS8 1RJ, UK

ABSTRACT

Caldera collapse events can be sudden and violent in the case of large explosive volcanic eruptions or incremental in the case of long-lived eruptions. Faults nucleating during collapse are associated with seismic activity, y~~but also can~~ also ~~host potential economic resources. Y~~et the ~~timing, location, and evolution~~kinematic behavior of newly formed faults ~~are~~ is poorly constrained. We conducted a series of novel sandbox experiments using ~~a series of~~ piezoelectric sensors to monitor stress perturbations during a caldera collapse. We found excellent spatial and temporal correlations among (a) fault nucleation, inferred from the stress sensor data, (b) the appearance of faults on the surface, and (c) final fault structure, obtained via cross-sections. We estimated fault propagation rates for early inner faults and found that these rates ~~are nonlinear and scale~~increase with ~~the~~increasing magma evacuation rates~~,~~. ~~which scale with the evacuation rates.~~ We applied our experimental results to seismic data from natural caldera-forming episodes in order to estimate rates of fault propagation for these systems. ~~We found that the fault propagation rate is both nonlinear and scales with the magma~~

~~evacuation rate.~~ Our experiments are consistent with en masse caldera collapse events, such as at Katmai in 1912 and Pinatubo in 1991.

INTRODUCTION

Calderas are large depressions found in all types of volcanic settings. ~~They are the relics of among the largest and most catastrophic volcanic events in a planet's history.~~ A caldera-forming eruption involves significant hazards on local, regional, and global scales, hence the importance to study and understand the mechanics of such events.

Faults ~~play a fundamental role~~ forming during ~~such~~ caldera collapses play a fundamental role as~~.~~ t~~T~~hey control the locations of the eruptive vents, as well as the nature and rate of caldera subsidence. ~~Their nucleation also releases vast amounts of potentially threatening seismic energy (e.g., Abe, 1992). The faults later provide a plumbing network for hydrothermal systems, generating economically important ore deposits as well as geothermal energy sources (e.g., Stix et al., 2003).~~

Notable advances in our knowledge of caldera formation have occurred in the past few decades, thanks to field (e.g., Geshi et al., 2002), experimental (e.g., Roche et al., 2000), theoretical (e.g., Roche and Druitt, 2001) and integrated studies (e.g., Stix and Kobayashi, 2008). Nevertheless, a number of fundamental problems have yet to be solved. When do faults nucleate at depth and how fast do they propagate? ~~At what point does subsidence shift from one set of faults to another?~~ How is seismic energy released from the caldera in a spatial and temporal sense?

~~Building upon previous studies (e.g., Roche et al., 2000; Walter and Troll, 2001; Kennedy et al., 2004; Burchardt and Walter, 2010), we~~We address these questions through a series of novel analogue experiments, ~~and~~ focussing on the effect of evacuation rate on the kinematics of collapse. We instrumented our experiments with a series of sensors designed to record fault development and energy release as a function of both time and space. We . . We then compare our results to historical caldera-forming events.

METHODOLOGY

Experimental Apparatus

Our experimental setup is composed of a 1-m diameter, 1.4-m height cylindrical tank filled with brown sand. We used a water-filled rubber bladder to represent the magma chamber. Once inflated, the bladder is an oblate ellipsoid 30 cm wide and 15 cm thick at the center, with an initial volume of 5 L. The bladder was buried so that its top was ~7 cm beneath the surface, thus yielding a roof aspect ratio (roof thickness / bladder diameter) of 0.23. These conditions represent a natural magma chamber whose roof lies at ~2 km below the surface. Full details of the experimental setup can be found in the Supplemental Material and in Coumans and Stix (2016).

We used piezoelectric sensors to monitor changes in the interior of our sandbox. The sensors feature piezoelectric transducers which produce an electric signal in response to differential stresses. Thus, our sensors record stress variations. Three sensors were placed on a horizontal line and buried about halfway between the top of the bladder and the surface. The first sensor was located directly above the center of the bladder and the other two were placed above the edge of the bladder. We refer to them as center, east and west sensors, respectively.

In running an experiment, water was pumped out of the bladder, simulating an eruption and triggering the caldera collapse. The evacuation rate was controlled so that, regardless of the duration of the experiment, the final volume of water evacuated from the bladder was 50% of the initial volume. After each experiment, we sectioned the caldera into to obtain pictures of cross sections.

Scaling Relations

Every parameter of the experiment was carefully scaled, to accurately reproduce natural caldera collapses (Sanford, 1959). For each fundamental dimension X, we define a ratio $X^* = X_{\text{model}} / X_{\text{nature}}$. Our length ratio is $L^* = 3.5 \times 10^{-5}$, so that our 35 cm calderas represent a 10 km diameter caldera in nature. Gravitational conditions are identical in nature and in our model, thus $g^* = L^*T^{*-2} = 1$, yielding a time scaling ratio of $T^* = (L^*)^{½} = 5.9 \times 10^{-3}$. Dry sand has a bulk density of 1650 kg m^{-3} whereas the density of volcanic rocks is ~2800 kg m^{-3}. Hence our density ratio is $\rho^* = 0.59$. The density ratio for the fluids (water with density of 1000 kg m^{-3} and magma with density of 2200 kg m^{-3}) is 0.45, which is within the same order of magnitude. The stress ratio is $\sigma^* = \rho^* g^* L^* = 2 \times 10^{-5}$. The natural cohesion of volcanic rocks is ~10^7 Pa (Hoek et al., 1995) but can be as low as 10^6 Pa (Schultz, 1996). It is difficult to precisely determine our sand cohesion, but it is safe to assume it is within 0–100 Pa, which is reasonable for our purpose. Finally the viscosity ratio is given by $\mu^* = \sigma^* T^* \approx 10^{-7}$. Since $\mu_{\text{water}} = 10^{-3}$ Pa s, this represents a natural magma with a viscosity of 10^4 Pa s.

Limitations

We focus solely on fault nucleation and propagation as the caldera develops, so our experiments did not include any pre-existing structural discontinuities, although they are present in nature because of magma chamber inflation or local tectonics. Furthermore, our experiments did not include any temperature, magma rheology, ring dykes or vent-migration effects, which can influence the collapse dynamics (e.g., Kennedy et al., 2008). However, our simplified approach allows us to focus on and isolate the caldera response to evacuation of the magma chamber. The stress changes recorded by the piezometers are not directly equivalent to ground motion recorded by seismometers at real calderas. Nevertheless, they provide a good approximation and guide to the locations of seismic events in nature. Lastly, our magma evacuation procedure did not include eruption and accumulation of material at the surface. Although such processes are likely to influence caldera subsidence, our procedure focuses directly upon how the roof of the reservoir responds to progressive evacuation of the reservoir.

RESULTS

A key objective was to compare fault development for a caldera which formed rapidly at relatively high evacuation rates versus one which formed more slowly at reduced evacuation rates. Hence the duration of our first experiment (A) was 2.5 min with an evacuation rate of 1 L min^{-1}; for the second experiment (B) the duration was 12.5 min with an evacuation rate of 0.2 L min^{-1}.

Both experiments followed the four general stages commonly observed and summarized by Acocella (2007). Deformation starts with broad sagging, before the first inner faults appear. Peripheral regions then start subsiding, and finally, outer faults appear on the surface. The output from the stress sensors is presented in Figure 1 for both experiments; the sensor units are arbitrary. For each experiment, we studied the most significant faults and noted the time at which they appeared on the surface. For experiment A, we picked the first fault appearing, the second inner fault, the eastern outer fault and the western outer fault. For experiment B, we used the first fault, the western outer fault and a large northwestern embayment. For both experiments, the first fault was the most obvious and significant feature as it appeared on the surface.

In experiment A, the signals from the three sensors are flat and steady before the experiment starts (Fig. 1a). All three sensors record a large offset as the experiment is initiated by the pump being turned on. The signals return to a flat, steady pattern after a few seconds. The first noticeable event occurs in the center sensor signal; after a few small spikes, a very large drop occurs, starting at 20.5 seconds. The first fault also appears in the central area between 23.5 and 24.5 s (Fig. 2a). This drop is followed by a positive signal peaking at ~33 s and then decaying for ~20 s. A second smaller peak is observed at ~56 s, and the second set of inner faults appear on the surface at 58–59 s. The center sensor signal then becomes flat, with progressively fewer perturbations until the end of the experiment. The east sensor is the next to record a period of unrest. From 75 s until the end of the experiment, the deviations from the baseline signal are much larger, with maximum amplitudes between 85 and 110 s. The eastern outer fault appears between 67 and 70 s. From 125 s until the end of the experiment, the west sensor shows a period of high activity relative to its baseline. This coincides with the appearance of the western outer fault at the surface between 117 and 120 s. Outer faults propagate all around the caldera until ~125 s. After this time, the caldera continues to deepen but ceases its outward growth. All three sensors return to their initial state after the experiment ends at 150 s.

In experiment B, the three sensor signals are flat before the start of the experiment. Large perturbations are observed as the experiment starts. At 55 s, the center sensor signal starts dropping and forms a very large trough with a minimum value at ~80

s. The first fault appears on the surface at 96–98 s. This is followed by a positive signal which peaks at 170 s, then slowly decays to ~415 s. The noise level is also much higher than beforehand, especially between 120 and 220 s. The west sensor records a period of activity starting at 500 s until the end. Western outer faults first appear between 406 and 410 s and then propagate very slowly. A large embayment appears on the northwestern edge between 491 and 495 s. By ~500 s, the caldera is well defined and stops propagating outward. It deepens, however, and the walls become more defined until the end of the experiment. The east sensor records a few medium amplitude peaks toward the end of the experiment but no large amplitude signal.

The stress field is not spatially uniform during an experiment (Roche et al., 2000). Thus, the polarity of the signal (Fig. 1) is an indicator of whether the sensor is experiencing compressive or tensile stresses.

For experiment A, we show a plan view of the final deformation pattern after the experiment (Fig. 2a) and a representative cross section (Fig. 2b). We use a color code in Figures 1 and 2 to illustrate fault development, in order to show (1) the faults' first appearance on the surface and the respective sensor response (Fig. 1a) and their respective location in the caldera (Fig. 2).

The final surface deformation is complex, with many small faults (Fig. 2a). However, the overall pattern is consistent with the results obtained by Kennedy et al. (2004). Our cross-sectional data (Fig. 2b) are also consistent with observations made by Kennedy et al. (2004). Inner faults are outward dipping whereas outer faults are inward dipping. The set of inner faults is complex with many subsurface branches. The outer

Publisher: GSA
Journal: GEOL: Geology
DOI:10.1130/G39551.1

faults accommodated significant displacement on both sides and do not exhibit branching.

In summary, there is a clear correlation between stress perturbations, as recorded by our sensors during the course of an experiment, and fault development at the surface. Most notably, the large early trough is followed shortly by the first appearance of the main inner fault at the surface.

FAULT EVOLUTION

Despite the different run times, the two experiments are broadly comparable in terms of fault development and caldera evolution~~. The general patterns of the signals in~~ (Figure 1a and 1b~~) are very similar for each sensor.~~. In both cases, the center sensor was the first to record significant events, namely a very large drop followed by a large peak. The west sensor exhibited very similar signals for both experiments, showing activity and instability near the end. For the east sensor, in experiment B there were very few perturbations compared to experiment A. This may be due to the fact that only a small amount of faulting developed on the eastern side of the caldera in experiment B. The style of collapse is therefore very close.

Fault nucleation processes are intimately related to stress perturbations. Faults are localized, irreversible ruptures. They form as a response to decompression of the magma chamber. Fault nucleation and propagation therefore produce a local, sudden stress drop. Our sensors record stress changes; thus, perturbations from the equilibrium state of the sensors are associated with fault nucleation sequences. This hypothesis is supported by the excellent correlation between (a) periods of large deviations relative to background in the sensor recordings and (b) fault formation observed at the surface. The correlation is spatial as well as temporal; when a fault appears at the surface, it is always the closest sensor that records significant variations. Furthermore, the sensors' response to stress variations decreases rapidly with distance, reinforcing the idea that the largest observed signals from a particular sensor are generated by faults forming closest to that sensor. It is thus possible to follow the stages of collapse from the signals in Figure 1. The collapse is initiated along an inner fault in the central area, consistent with major changes in the center sensors stress signals, while the outer sensors record nothing. The outer faults form asymmetrically; they start nucleating on one side before propagating to the other. This behavior is particularly visible in experiment A for which our visual observations suggest that collapse is initiated on the east side and then propagates to the west. This is again consistent with the data in Figure 1a where the east sensor records high stress changes beginning at ~70 s, while the west sensor does not record any instability until ~110 s.

We observe two distinct faulting patterns in the stress signal (Fig. 1). On one hand, the appearance of inner faults at the surface are preceded by a large, single peak in the sensor signal. By contrast, outer faults are not associated with any stress deviation before they appear on the surface, but they are followed by intense stress fluctuations. These contrasting stress patterns can be explained by distinct fault dynamics.

Inner faults propagate from the top of the magma chamber upwards, whereas outer faults nucleate at the surface and propagate downwards. This difference has been well documented (e.g., Roche et al., 2000; Kennedy et al., 2004; Acocella, 2007; Burchardt and Walter, 2010). It is confirmed in our experiments by observing how the amount of displacement accommodated by each fault varies with depth (see Supplementary Material). The direction of propagation therefore explains why inner faults are recorded in the stress signal before they are visible at the surface, while outer faults exhibit stress perturbations only after they nucleate at the surface and propagate downward.

Inner and outer faults also exhibit two distinct growth modes (see Supplementary Material). The large and abrupt peaks associated with inner faults suggest a rapid and sudden fault development. By contrast, outer faults produced several smaller peaks in the stress signal for a longer period. This indicates slower, more incremental fault growth.

By indicating when faults nucleate, our sensor data give us insight on where and when earthquakes occur during subsidence. The center sensor records sudden, large stress changes, suggesting en masse caldera collapse at an early stage of caldera evolution. These data resemble those for collapse at Katmai in 1912 and Pinatubo in 1991 (Stix and Kobayashi, 2008). In these natural collapses, large amounts of seismic energy were suddenly released about halfway through the eruptions. The largest signals we observed are the first very large drops recorded by the center sensor in both experiments. This would thus correspond to the largest seismic events, followed later by smaller magnitude earthquakes, corresponding to events recorded by the east and west sensors. In our experiments, the largest events occur after less than 10% of the reservoir volume is evacuated, as opposed to midway through the climactic eruption sequence as observed at Katmai and Pinatubo. This is due to the different aspect ratios involved (roof thickness / magma chamber diameter). Our experiments had an aspect ratio of 0.23 whereas Katmai and Pinatubo have aspect ratios of 2.0 and 2.4, respectively. At higher aspect ratios, faults form later (Roche et al., 2000), delaying seismic events.

Stix and Kobayashi (2008) showed that this sudden, en masse collapse behavior contrasts strongly with a longer, more continuous style of collapse, as observed at Miyakejima (Japan, Geshi et al., 2002) in 2000, and Bárðarbunga (Iceland, Gudmundsson et al., 2016) in 2014–2015. This latter style of collapse involves (a) basaltic magma as opposed to the more silicic magmas of Katmai and Pinatubo, and (b) slower magma evacuation rates (1.7×10^2 and 1.2×10^2 m^3 s^{-1} for Miyakejima and Bárðarbunga, respectively, compared to 2.2×10^5 and 3.6×10^5 m^3 s^{-1} for Katmai and Pinatubo, respectively). The end result is a protracted and progressive style of collapse. Future experimental work could easily model this behavior and examine detailed stress perturbations under these conditions.

FAULT PROPAGATION

By focusing on ~~both~~ the timing of both the first sharp drop in the sensor signal~~,~~ and the associated fault's appearance at the surface~~, and the associated sharp drop in the sensor signal~~, we can estimate the rate of fault propagation from the magma chamber to the surface. First, we measure the time delay Δt between the beginning of the drop in the sensor signal and the fault's appearance at the surface. Inner faults nucleate on top of the magma chamber and propagate upward. Knowing the depth of the top of the magma chamber h, we can then compute the model propagation rate $R_{model} = h/\Delta t$, which is 0.023 ± 0.005 m s^{-1} for experiment A and 0.00168 ± 0.00004 m s^{-1} for experiment B. We then scale back to natural speeds using $R_{nature} = R_{model}/R^*$, where R^* is the propagation rate scaling ratio given by $R^* = L^*T^{*-1}$. This scaling up produces fault propagation rates for natural systems of 3.8 m s^{-1}, based on experiment A, and 0.28 m s^{-1}, based on experiment B. A higher evacuation rate therefore yields a higher fault propagation rate.

DOI:10.1130/G39551.1

We can now apply these propagation rates to natural settings at Katmai and Pinatubo and compare our estimates to real seismic data. Propagation rates depend on evacuation rates, hence, to choose the appropriate propagation rate for natural systems, we ~~now~~ scale ~~up~~ our experimental evacuation rates E_{model} back to natural values E_{nature} using $E_{nature} = E_{model}/E^*$ and the scaling ratio $E^* = L^{*3}T^{*-1}$ ~~and $E_{nature} = E_{model}/E^*$~~ (see Scaling Relations section). Values for E_{nature} are 2.3×10^6 m^3 s^{-1} and 4.6×10^5 m^3 s^{-1} based respectively on experiments A and B. The ~~second~~ value from experiment B is similar to observed evacuation rates ~~for~~ at Katmai and Pinatubo (2.2–3.6 × 10^5 m^3 s^{-1}). Hence we apply a fault propagation rate of 0.28 m s^{-1} ~~for~~ to natural systems.

In the case of Katmai, the top of the magma chamber was 4–5 km beneath the surface (Hildreth and Fierstein, 2000). Based on this depth and our chosen fault propagation rate of 0.28 m s^{-1}, we obtain a time interval of 238–298 min for faults nucleating at the top of the magma chamber to reach the surface. This timescale can be compared with the occurrence of earthquakes at Katmai. The largest earthquakes occurred on 8 June 1912 between 0611 and 1300 h UTC, representing an elapsed time of 409 min. This interval is comparable to our experimental data and scaling analysis, suggesting that the major caldera-forming fault system at Katmai was established and complete, from the top of the magma chamber to the surface, within 6.8 h, resulting in caldera subsidence.

For Mount Pinatubo, the top of the magma chamber was ~6 km deep (Mori et al., 1996). According to our analysis, it would then take 357 min for a fault to propagate all the way to the surface. During the climactic eruption on 15 June 1991, the largest seismic events of M5 and greater occurred from 0739 to 1225 h UTC, yielding a total elapsed time of 286 min. However, the bulk of seismic energy was released over a comparatively short interval of 51 min stretching from 1041 to 1132 UTC. This observation suggests that both the fault propagation rate and magma evacuation rate were unusually high during this time. This is not surprising, since the evacuation rate likely undergoes substantial variations during such eruptions. Despite the aspect ratio difference, the elevated evacuation rates in our experiments and for our natural examples (Katmai and Pinatubo) indicate a specific sequence of fault growth. The principal inner faults, which form rapidly, contrast with the longer durations and timescales of the outer faults. This dichotomy may be explained as a drawn-out response of the outer faults to sudden, large-scale fault movement in the central region of the caldera. Furthermore, significant seismicity may occur under certain conditions after the climactic eruption. In our experiments, all stress perturbations and faulting ceased when the pump was turned off. In nature, however, some further magma evacuation may be expected to occur after the large eruption from a series of smaller eruptions, subsurface magma drainage, or both. A certain threshold may be reached which causes further subsidence and associated earthquakes. This was observed at both Katmai and Pinatubo.

CONCLUDING REMARKS

Using piezoelectric sensors in a series of analogue caldera collapse experiments, we were able to document stress perturbations of en masse caldera collapses similar to natural events such as at Katmai in 1912 and Pinatubo in 1991. Our results provide insight on the timing, location, and evolution of fault nucleation. This new and original experimental technique may be used to model other kinematic behaviors. We also estimated the propagation rate of early inner faults. This type of information is essential

Publisher: GSA
Journal: GEOL: Geology
DOI:10.1130/G39551.1

for our understanding of seismicity and fault development during caldera formation and, ultimately, our ability to assess and mitigate hazards in such settings.

ACKNOWLEDGMENTS

We thank Joan Martí, Nobuo Geshi, Valerio Acocella and an anonymous reviewer for their constructive comments. We would also like to thank Jason Coumans for his help in setting up these experiments. This work was funded by Discovery and Accelerator grants to JS from the Natural Sciences and Engineering Research Council of Canada.

REFERENCES CITED

~~Abe, K., 1992, Seismicity of the caldera-making eruption of Mount Katmai, Alaska in 1912: Bulletin of the Seismological Society of America, v. 82, p. 175–191.~~

Acocella, V., 2007, Understanding caldera structure and development: An overview of analogue models compared to natural calderas: Earth-Science Reviews, v. 85, p. 125–160, https://doi.org/10.1016/j.earscirev.2007.08.004.

Burchardt, S., and Walter, T.R., 2010, Propagation, linkage, and interaction of caldera ring-faults: comparison between analogue experiments and caldera collapse at Miyakejima, Japan, in 2000: Bulletin of Volcanology, v. 72, p. 297–308, https://doi.org/10.1007/s00445-009-0321-7.

Coumans, J.P., and Stix, J., 2016, Caldera collapse at near-ridge seamounts: an experimental investigation: Bulletin of Volcanology, v. 78, p. 70–89, https://doi.org/10.1007/s00445-016-1065-9.

Geshi, N., Shimano, T., Chiba, T., and Nakada, S., 2002, Caldera collapse during the 2000 eruption of Miyakejima Volcano, Japan: Bulletin of Volcanology, v. 64, p. 55–68, https://doi.org/10.1007/s00445-001-0184-z.

Gudmundsson, M.T., et al., 2016, Gradual caldera collapse at Bárdarbunga volcano, Iceland, regulated by lateral magma outflow: Science, v. 353, p. 262–270, https://doi.org/10.1126/science.aaf8988.

Hildreth, W., and Fierstein, J., 2000, Katmai volcanic cluster and the great eruption of 1912: Geological Society of America Bulletin, v. 112, p. 1594–1620, https://doi.org/10.1130/0016-7606(2000)112<1594:KVCATG>2.0.CO;2.

Hoek, E., Kaiser, P.K., and Bawden, W.F., 1995, Support of underground excavations in hard rock: A.A. Balkema, Rotterdam, Netherlands, p. 215.

Kennedy, B., Stix, J., Vallance, J.W., Lavallée, Y., and Longpré, M.-A., 2004, Controls on caldera structure: Results from analogue sandbox modeling: Geological Society of America Bulletin, v. 116, p. 515–524, https://doi.org/10.1130/B25228.1.

Kennedy, B.M., Jellinek, A.M., and Stix, J., 2008, Coupled caldera subsidence and stirring inferred from analogue models: Nature Geoscience, v. 1, p. 385–389, https://doi.org/10.1038/ngeo206.

Mori, J., Eberhart-Phillips, D., and Harlow, D.H., 1996, Three-dimensional velocity structure at Mount Pinatubo: resolving magma bodies and earthquake hypocenters, *in* Newhall, C.G., and Punongbayan, R.S., eds., Fire and mud: eruptions and lahars of Mount Pinatubo, Philippines: Quezon City, Philippines, Philippine Institute of Volcanology and Seismology, and Seattle, Washington, University of Washington Press, p. 371–382.

Roche, O., and Druitt, T.H., 2001, Onset of caldera collapse during ignimbrite eruptions: Earth and Planetary Science Letters, v. 191, p. 191–202, https://doi.org/10.1016/S0012-821X(01)00428-9.

Roche, O., Druitt, T.H., and Merle, O., 2000, Experimental study of caldera formation: Journal of Geophysical Research. Solid Earth, v. 105, p. 395–416, https://doi.org/10.1029/1999JB900298.

Sanford, A.R., 1959, Analytical and experimental study of simple geologic structures: Geological Society of America Bulletin, v. 70, p. 19–52, https://doi.org/10.1130/0016-7606(1959)70[19:AAESOS]2.0.CO;2.

Schultz, R.A., 1996, Relative scale and the strength and deformability of rock masses: Journal of Structural Geology, v. 18, p. 1139–1149, https://doi.org/10.1016/0191-8141(96)00045-4.

~~Stix, J., Kennedy, B., Hannington, M., Gibson, H., Fiske, R., Mueller, W., and Franklin, J., 2003, Caldera-forming processes and the origin of submarine volcanogenic massive sulfide deposits: Geology, v. 31, p. 375–378, https://doi.org/10.1130/0091-7613(2003)031<0375:CFPATO>2.0.CO;2.~~

Stix, J., and Kobayashi, T., 2008, Magma dynamics and collapse mechanisms during four historic caldera-forming events: Journal of Geophysical Research, v. 113, p. B09205, https://doi.org/10.1029/2007JB005073.

~~Walter, T.R., and Troll, V.R., 2001, Formation of caldera periphery faults: An experimental study: Bulletin of Volcanology, v. 63, p. 191–203, https://doi.org/10.1007/s004450100135.~~

FIGURE CAPTIONS

Figure 1. Stress evolution during (a) experiment A and (b) experiment B. The times at which faults of interest appear on the surface are indicated.

Figure 2. (a) Final surface deformation of experiment A, viewed from above with lighting from the west. Faults are highlighted. (b) Cross section of experiment A. The plane of view is indicated in (a). Faults are highlighted. The former surface of the experiment is shown in red.

1GSA Data Repository item 2017xxx, xxxxxxxx, is available online at http://www.geosociety.org/datarepository/2017/ or on request from editing@geosociety.org.